

Benchmarking of Stability and Robustness against Grid Impedance Variation for LCL-Filtered Grid-Interfacing Inverters

Minghui Lu, *Member, IEEE*, Ahmed Al-Durra, *Senior Member, IEEE*, S.M. Muyeen, *Senior Member, IEEE*, Siyu Leng, *Member, IEEE*, Poh Chiang Loh, *Frede Blaabjerg, Fellow, IEEE*

Abstract—This paper comprehensively analyzes the stability of a grid-interfacing inverter with LCL-filter in the discrete domain, where the LCL-filter, along with the controller, are modeled in a polar coordinate. System open-loop and closed-loop poles are analytically studied and expressed in the z-domain. Through the poles movement and distribution analysis, the relationship between system stability and the ratio of resonance frequency over sampling frequency is mathematically revealed and calculated as well as the system control gain limit. Moreover, this paper demonstrates that grid-voltage feedforward regulator would significantly alter the inverter stability in a weak power system. By means of Jury stability criterion, the stability status under different filter resonance frequency is given. The selection of resonance frequency and filter parameters makes a considerable difference on system behavior. Finally, to improve the robustness against grid inductance variation, a conservative design recommendation of filter parameters and control gain is given. Through the tests on a laboratory-scale prototype, the theoretical analysis is validated by experimental results.

Index Terms—Grid-connected converters, LCL-filter, stability analysis, robust assessment.

I. INTRODUCTION

With the development of highly penetrated renewable energy generation systems, grid-connected inverters have been extensively employed as flexible and efficient grid interfaces in the modern power system [1]. These converters are able to realize efficient power conversion between renewables and grid, but they also bring the resonance and instability problems at the same time [2]. Hence, many innovative schemes have been developed to attenuate the undesirable resonances and to avoid the system instability [3], [4]. It is still a big challenge for researchers and engineers how to maintain high performance of power converters in the complex grid conditions, for instance the power grid is weak or contains background voltage harmonics.

To properly filter out switching frequency harmonics, LCL-filters are usually placed between the inverter and the grid to obtain high quality grid current [5], [6]. However, the control of a grid-connected inverter with LCL-filter remains to be quite a challenging task, since the LCL network causes a resonance near to the control boundary [7]. Either the grid-side or inverter-side current can be controlled, each alternative has its own advantages and shortcomings depending on specific applications [6]. [8] and [9] demonstrates the interrelationships between grid-side current control and inverter-side current control through graphic block

diagram derivation. In recent literatures [4], [10]-[15], stable operation of LCL-filtered inverter without any additional damping has been proved to be possible. The simple and effective single loop control with typical linear Proportional Integral (PI) or Proportional Resonant (PR) controllers are promising options for industrial applications. [10] explores the inherent damping characteristic of LCL-filters when the inverter-side current is controlled. In [11], it reveals that the grid-side current feedback control attenuates the resonance introduced by LCL-filters due to the inherent damping feature embedded in the control loop. It has been found that the essential reasoning for stable operation are the critical role of time delays in stabilizing the grid connected inverters, which have been discussed a lot in LCL-filtered grid-connected applications [12]-[15]. The *critical frequency* concept is first proposed in [13] to identify the stable region and unstable region. It has been demonstrated that one sixth of the sampling frequency ($f_s/6$) is the critical resonance frequency when one sample delay is considered.

Besides stable operation, for the grid-connected inverters, the quality of the grid injected current is another matter of concern. How to keep high performance of grid-interfacing inverters attracts much research attention, especially when the power grid is weak and contains background harmonics. To obtain high robustness against grid inductance variation, [16] proposes an optimized controller design for grid-interfacing inverters, a specific gain for capacitor-current-feedback active damping is selected to achieve the goal. The similar conclusion is illustrated through passivity-theory for the inverter-side current control [17]. Moreover, [8], [18], [19] demonstrate that a reduced time delay in the digital controller would improve system robustness and enhance system stability for the grid-current feedback control. To better adapt to high grid impedance power grid, [20] shapes the output impedance of the grid-connected inverter through the comparison of parallel impedance and series impedance.

On the other hand, to suppress the injected grid current distortion caused by the grid voltage harmonics, two methods are commonly adopted: 1) Current regulator plus selective harmonics compensation with multiple PR regulators [21], [22], 2) A feedforward scheme of grid voltage [24]-[31]. Compared to the former, the Grid Voltage Feedforward Regulator (GVFR) demonstrates the advantages of simplicity, wider bandwidth, and better dynamic performance. In [24], the concept of harmonic impedance is proposed to discuss the

issues of the output current distortion, and a capacitor-current feedforward controller is designed to dispense the output admittance. Basically, the reason for the grid current distortion is that the output admittance provides a path to the grid voltage harmonics. A *full-feedforward* concept is proposed in [25] and [26] to fully eliminate the output admittance. However, multiple and high order derivative elements are introduced, which are sensitive to noises, making it difficult for practical implementation. In industrial applications, especially for the high-power cases, the proportional GVFR is still widely used. In [27]-[29], it is reported that the feedforward control improves system stability for LCL-filtered inverter when the inverter side current is controlled. The grid voltage feedforward control can bring an inherent damping characteristic under the approximation that the digital delay block is replaced by first order Taylor series [27]. On the contrary, [30] claims that the feedforward voltage will result in a positive grid current feedback, which essentially degrades the system stability and control performance. In view of the above issues, a comprehensive analysis for GVFR remains undeveloped yet. Therefore, it is necessary to have a more comprehensive discussion on the impacts of the grid voltage feedforward control on the system stability with weak grid situations taken into consideration.

This paper investigates the stability of a grid-interfacing inverter with LCL-filter in the discrete domain, where the LCL-filter, along with the controller, are modeled in a polar coordinate. To improve the system robustness against grid-impedance variation, a robust design of LCL-filter and controller is presented. This paper starts with a pole distribution analysis for current loop in § II. In § III, by using the similar poles distribution analysis, the impacts of the GVFR on system stability are revealed; § IV analyzes the system robustness against grid inductance variation. § V recommends a conservative LCL-filter design method to improve adaptability to the weak grid condition. A robust design area for filter capacitance selection is calculated and graphically illustrated; § VI then finalizes the paper by showing the verified experiment results.

II. MODELING AND STABILITY ANALYSIS OF LCL-FILTERED GRID-CONNECTED INVERTER

In this study, current control implementation in stationary coordinates (the $\alpha\beta$ frame) is assumed here. Therefore, the conclusions investigated are applicable not only to single-phase systems, but also to per-phase control of multiphase systems.

A. Modeling

Fig. 1 shows a voltage source converter (VSC) connected to the grid through an LCL-filter. L_1 is the inverter-side inductor, C is the filter capacitor and L_2 is the grid-side inductor, L_g is the grid inductor. The inner resistance of L_1 , L_2 and L_g are neglected to emulate the worst case. The grid current i is sampled and controlled through a linear controller with the transfer function $G_c(s)$.

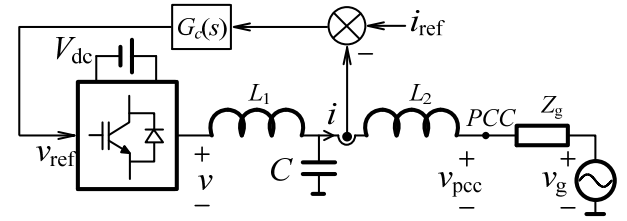


Fig. 1. Topology and current control architecture of a LCL-filtered grid-connected inverter.

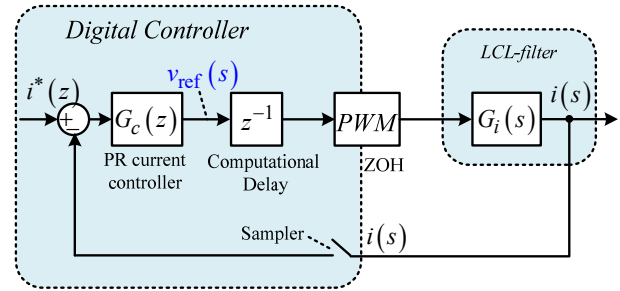


Fig. 2. Implementation of digital controller in an LCL-filtered converter.

Digital control implementation is assumed here, where the sampling is carried out synchronously with the converter switching. The PWM process is assumed always to operate within the linear range limited by the dc-link voltage [6]. The nonlinear effects are out of scope and will not be discussed in this paper. To illustrate, the control block diagram is represented in Fig. 2, where the LCL-filter has been modelled in the s -domain and the digital controller has been notated in the z -domain. Between the LCL-filter and digital controller are the sampler and pulse-width modulator, which together with the non-zero computational time, will introduce a total delay of 1.5 times the sampling period T_s [17]. A pure time delay suffices as a converter model as

$$v = e^{-sT_d} \cdot v_{\text{ref}}, \quad T_d = 1.5T_s \quad (1)$$

The system plant can be obtained where the function $G_i(s)$ for relating the converter output voltage v to the grid current i , as shown in Fig. 1, can be derived as

$$G_i(s) = \frac{i(s)}{v(s)} = \frac{1}{sL_1L_tC} \frac{1}{s^2 + \omega_r^2}, \quad L_t = L_2 + L_g \quad (2)$$

where ω_r is the filter resonance frequency expressed as

$$\omega_r = \sqrt{\frac{L_1 + L_t}{L_1L_tC}} \quad (3)$$

Compared to L-filtered system, a resonant part is undesirably introduced in the LCL-filtered system as shown in (2), which may make the system oscillatory, or even unstable. The study in this paper is executed in the z -domain. The s -domain transfer function $G_i(s)$ can next be transformed to z -domain by applying zero-order-hold (ZOH) discretization

method. The resulting function, shown in Fig. 3 as $G_i(z)$, is given as (4), where T_s represents the sampling period of the digital control system.

$$G_i(z) = \frac{\omega_r T_s [z^2 - 2z \cos(\omega_r T_s) + 1] - \sin(\omega_r T_s)(z-1)^2}{\omega_r (L_1 + L_2 + L_g)(z-1)[z^2 - 2z \cos(\omega_r T_s) + 1]} \quad (4)$$

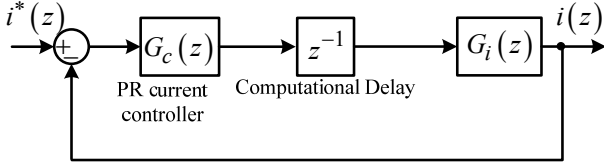


Fig. 3. Circuit and control block diagram in the z -domain.

Besides, the current controller $G_c(s)$ should also be discretized. The Proportional Resonant (PR) controller [23] is widely adopted in grid-connected application, whose transfer functions before and after pre-warped Tustin transformation [32] are written in (5) and (6), respectively. In both expressions, K_p is the proportional gain, whereas K_i is the resonant gain. Also included is the fundamental angular frequency ω_b , where the final steady-state tracking error will be zero. The knowledge and design methods of the PR controller are presently well-known, and will not be further elaborated.

$$G_c(s) = K_p + \frac{K_i s}{s^2 + \omega_b^2} \quad (5)$$

$$G_c(z) = K_p + \frac{K_i \sin(\omega_b T_s)}{2\omega_b} \frac{z^2 - 1}{z^2 - 2z \cos(\omega_b T_s) + 1} \quad (6)$$

As Fig.3, the open-loop transfer function $T_{i-1}(z)$ can eventually be obtained through merging forward path, including the PR controller $G_c(z)$, digital delay z^{-1} and the system plant $G_i(z)$. The open loop transfer function $T_{i-1}(z)$ is written as

$$T_{i-1}(z) = G_c(z) \cdot z^{-1} \cdot G_i(z) = \frac{G_c(z)}{\omega_r (L_1 + L_2 + L_g)} \cdot \frac{\omega_r T_s [z^2 - 2z \cos(\omega_r T_s) + 1] - \sin(\omega_r T_s)(z-1)^2}{z \cdot (z-1) \cdot [z^2 - 2z \cos(\omega_r T_s) + 1]} \quad (7)$$

B. Poles Distribution

The system poles can be analyzed through the denominator of equation (7). Apart from two poles introduced by the PR controller, another four open-loop poles z_1, z_2, z_3, z_4 can be identified, which includes two fixed poles at original point $z_1 = 0$ and $z_2 = 1$, together with two resonant poles z_3, z_4 as shown in (8) and (9).

$$z_1 = 0, z_2 = 1 \quad (8)$$

$$z_{3,4} = \cos(\omega_r T_s) \pm j \cdot \sin(\omega_r T_s) = e^{\pm j\omega_r T_s} \quad (9)$$

To be emphatically pointed out, the resonant poles z_3, z_4 are the conjugate roots of equation $z^2 - 2z \cos(\omega_r T_s) + 1 = 0$, and can be expressed using exponential function with unity magnitude and phase changing with $\omega_r T_s$. The location and locus of these resonant poles can be plotted in a polar coordinate as shown in Fig. 4, where the resonant poles z_3, z_4 track along the edge of unit circle.

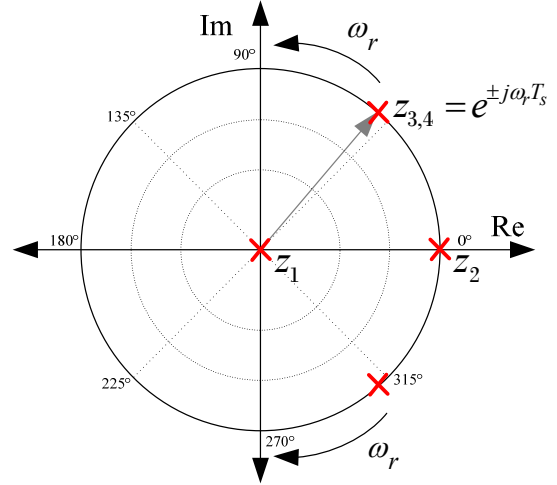


Fig. 4. Poles location in a polar coordinate of a voltage source converter with LCL-filter.

Although system stability is determined by the location of closed-loop poles instead of the open-loop ones, open-loop poles are starting points of closed-loop ones when the control gain K_p is equal to zero. Meanwhile, the open-loop poles $z_{3,4}$ are floating with $\omega_r T_s$. It indicates that system stability indirectly depends on the term $\omega_r T_s$ ($\omega_r T_s = 2\pi \cdot \omega_r / \omega_s$). Therefore, the ratio γ between the resonance frequency ω_r and sampling frequency ω_s , as expressed in (10), has significant impact on system stability.

$$\gamma = \frac{\omega_r}{\omega_s} \quad (10)$$

To verify the analysis above, Fig. 5 shows the root loci with three ratios γ sets ($\gamma_1=0.15, \gamma_2=0.24, \gamma_3=0.36$) for recognizing the role of the ratio γ playing on the poles distribution. Obviously, the three plots have totally distinct poles distribution, hence, also different system stability.

Plot (a) with $\gamma_1=0.15$ presents an unstable system regardless of the proportional gain K_p , while plot (b) and (c) present a conditionally stable system if K_p is properly selected. Obvious differences exit for these three cases. To analyze these differences, the closed-loop transfer function $H(z)$ is derived from $T_{i-1}(z)$ as

$$H(z) = \frac{T_{i-1}(z)}{1 + T_{i-1}(z)} \quad (11)$$

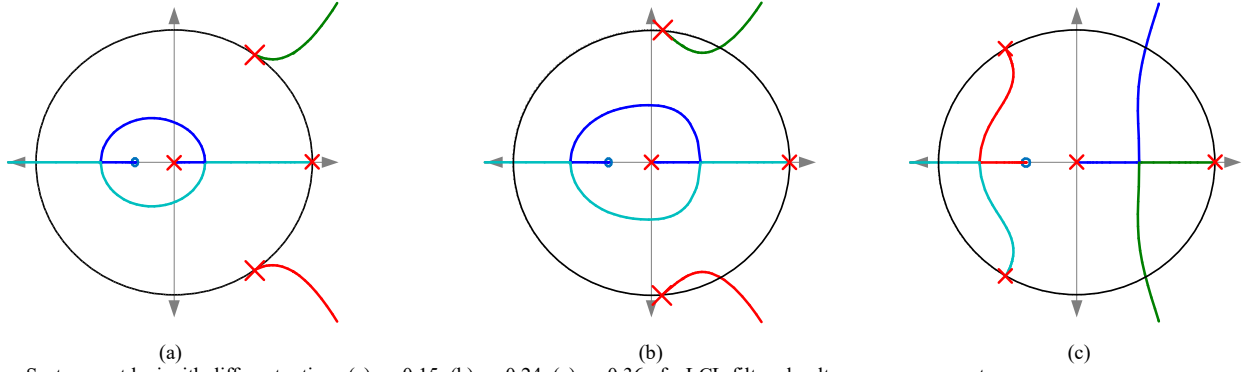


Fig. 5. System root loci with different ratio γ : (a) $\gamma_1=0.15$; (b) $\gamma_2=0.24$; (c) $\gamma_3=0.36$ of a LCL-filtered voltage source converter.

The denominator polynomial $P(z)$ of the closed-loop transfer function $H(z)$ is expressed in (12). Then, the system poles are those roots of equation $P(z)=0$. It is worth to note that all the root loci plots track through the unit circle at the same point as they become unstable, which can be identified as $z_c = 1/2 \pm j\sqrt{3}/2$. This recognition can be confirmed using simple geometry and can then be used to develop a fundamental gain limitation for controller design [13]. Substituting z_c into $P(z) = 0$, the proportional gain limitation K_{p_lim} for the controller design, as written in (13), can be calculated.

$$P(z) = \omega_r(L_1 + L_t) \cdot z \cdot (z-1) \cdot [z^2 - 2z \cos(\omega_r T_s) + 1] + K_p \left\{ \omega_r T_s [z^2 - 2z \cos(\omega_r T_s) + 1] - \sin(\omega_r T_s)(z-1)^2 \right\} \quad (12)$$

The limit value for the control gain can be derived from (12). From its expression, it is known that the K_{p_lim} value is a function of term $\omega_r T_s$.

$$K_{p_lim} = \omega_r(L_1 + L_t) \cdot \frac{1 - 2 \cos(\omega_r T_s)}{\sin(\omega_r T_s) + \omega_r T_s \cdot (1 - 2 \cos(\omega_r T_s))} \quad (13)$$

C. Critical Frequency and Control Limit

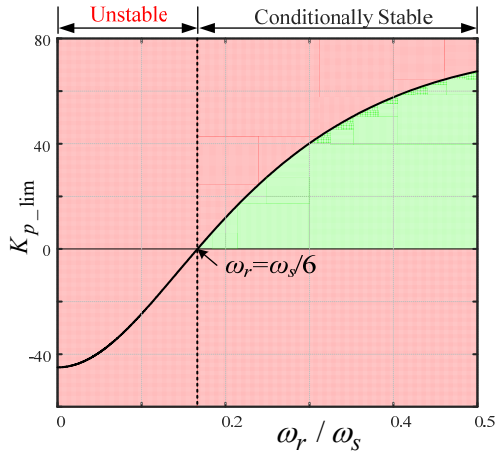


Fig. 6. Relationship between K_{p_lim} and ratio γ for the voltage source converters with LCL-filter.

According to control gain limit in (13), the relationship between the gain limit K_{p_lim} and the ratio γ is obtained and

plotted in Fig. 6, where the K_{p_lim} value changes sign from negative to positive at $\omega_r = \omega_s/6 \approx 0.167\omega_s$, which is defined as *critical frequency*. To be precise, the curve crosses over zero at the right point where the numerator term $1 - 2\cos(\omega_r T_s)$ equalizes to zero.

From the curve in Fig. 6, for $\omega_r/\omega_s < 1/6$ region, a negative control gain is required to stabilize the system. Obviously, it is not practical because the control gain in a control system is always selected above 0. Therefore, for $\omega_r/\omega_s < 1/6$ region, the system is unstable. The grid-connected system will be, on the other hand, conditionally stable only if the control gain is selected within the control gain limit.

III. STABILITY IDENTIFICATION OF THE SITUATION WITH GRID VOLTAGE FEEDFORWARD REGULATOR

Grid Voltage Feedforward Regulator (GVFR) is widely used to improve grid-connected system dynamic performance and mitigate the grid voltage background harmonics. To evaluate the potential impact of GVFR on the system stability, continued analysis following the previous section on poles distribution will be executed next.

A. Modeling

Compared with Fig. 1, an additional feedforward regulator $F(s)$ is inserted in Fig. 7. For the selection of $F(s)$, [25] proposed a *Full-Feedforward* controller for LCL-filtered inverters, it improves the high-order harmonics mitigation performance compared to the traditional solution of applying a unity feedforward gain. However, a high order controller is necessary, including a second order derivative term which is quite sensitive to noise. It might lead to difficulties in practical applications. In this study, a traditional solution with unity feedforward gain is considered $F(s) = 1$.

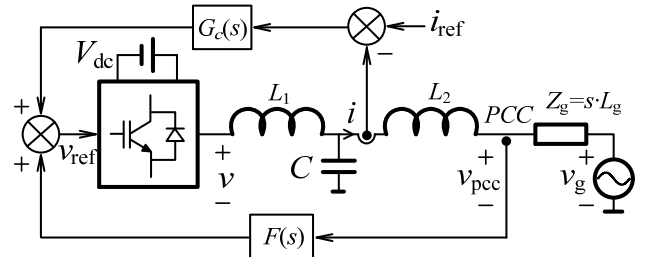


Fig. 7. Circuit and block diagram with grid-voltage feedforward regulator.

The function for relating the converter output voltage v to the PCC voltage can be derived as:

$$G_{pcc}(s) = \frac{v_{pcc}(s)}{v(s)} = \frac{L_g}{L_1(L_2 + L_g)Cs^2 + \omega_r^2} \quad (14)$$

where L_g is the series grid impedance in the grid.

Similarly, the continuous-domain transfer function can be transformed to the discrete-domain by applying ZOH discretization. The resulting function, notated in Fig. 8 as $G_{pcc}(z)$, is given as follows.

$$G_{pcc}(z) = \frac{L_g}{L_1 + L_2 + L_g} \frac{(z+1)(1 - \cos(\omega_r T_s))}{z^2 - 2z \cos(\omega_r T_s) + 1} \quad (15)$$

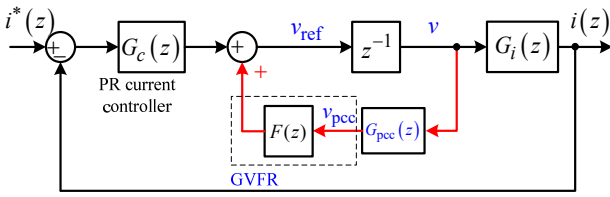


Fig. 8. Control block diagram in z-domain with GVFR.

The blocks in Fig. 8 can eventually be merged to give open-loop transfer function $T_{i_2}(z)$ as

$$T_{i_2}(z) = \frac{G_c(z)}{\omega_r(L_1 + L_2 + L_g)} \frac{\omega_r T_s [z^2 - 2z \cos(\omega_r T_s) + 1] - \sin(\omega_r T_s)(z-1)^2}{(z-1) \cdot \{z \cdot [z^2 - 2z \cos(\omega_r T_s) + 1] - k_a(z+1)(1 - \cos(\omega_r T_s))\}} \quad (16)$$

where k_a is a coefficient related to $F(z)$ with the expression as

$$k_a = \frac{L_g}{L_2 + L_g} \cdot \frac{F(z)}{L_1 C \omega_r^2} \quad (17)$$

Compared to the transfer function in (7) without GVFR, (16) has the same form except the additional term. Therefore, it can be observed that an additional GVFR $F(z)$ will definitely modify the system characteristic polynomial, which also certainly results in the system stability alteration.

According to the expression, in case that the grid inductance L_g is equal to 0, then $k_a = 0$, indicating that the GVFR would have no impact on the inverter system stability under stiff grid condition. On the contrary, if the grid inductance L_g is a non-zero value, i.e., the power system is weak, in some cases, varying within a large range of possible grid conditions in terms of stiffness [33]. The situation is particularly critical in rural areas where the distributed generation plants are connected due to many good natural resources, like solar or wind [33]. Then, the system stability is altered if the GVFR is added, and then do need more investigation.

B. Open-Loop Poles Analysis through Jury's Criterion

Fundamentally, the characteristic polynomial of (16), which

is expressed $D(z)$ as (18), plays a crucial role in the poles distribution. Because the roots of $D(z)$ are exactly the system poles, including a fixed one $z_1=1$ determined by term $(z-1)$ and other three poles are determined by the rest part of $D(z)$, written as $D_1(z)$ in (19).

$$D(z) = (z-1) \cdot \{z \cdot [z^2 - 2z \cos(\omega_r T_s) + 1] - k_a(z+1)(1 - \cos(\omega_r T_s))\} \quad (18)$$

To calculate the roots of $D_1(z)$ and analyze the distribution of the poles, the Jury's criterion [34], [35] is adopted, $D_1(z)$ is rewritten as the descending power series.

$$D_1(z) = z \cdot [z^2 - 2z \cos(\omega_r T_s) + 1] - k_a(z+1)(1 - \cos(\omega_r T_s)) \quad (19)$$

$$= a_0 \cdot z^3 + a_1 \cdot z^2 + a_2 \cdot z + a_3$$

where the coefficients can be written as:

$$\begin{cases} a_0 = 1 \\ a_1 = -2 \cdot \cos(\omega_r T_s) \\ a_2 = 1 - k_a + k_a \cdot \cos(\omega_r T_s) \\ a_3 = k_a \cdot \cos(\omega_r T_s) - k_a \end{cases} \quad (20)$$

Then the Jury table is constructed as follows:

Row	z^0	z^1	z^2	z^3
1	a_3	a_2	a_1	a_0
2	a_0	a_1	a_2	a_3
3	b_2	b_1	b_0	-

That is, the first row is constructed of the polynomial coefficients in order, and the second row is the first row in reverse order and conjugated. The third row of Table I are calculated as

$$b_2 = \begin{vmatrix} a_3 & a_0 \\ a_0 & a_3 \end{vmatrix}, b_1 = \begin{vmatrix} a_3 & a_1 \\ a_0 & a_2 \end{vmatrix}, b_0 = \begin{vmatrix} a_3 & a_2 \\ a_0 & a_1 \end{vmatrix} \quad (21)$$

The expansion of the table is continued in this manner until a row containing only one non-zero element is reached. In short, the polynomial $D_1(z)$ has all three roots inside of the unit circle if and only if the following requirements are met:

- $|a_3| < a_0$;
- $D_1(z)|_{z=1} > 0$;
- $D_1(z)|_{z=-1} < 0$;
- $|b_2| > |b_0|$.

From (20) and (21), the elements $a_0 \dots a_3$, $b_0 \dots b_2$ are the functions of k_a and ω_r , both of which are dependent on the feedforward gain $F(z)$ and the LCL-filter parameters. Consequently, the selection of the feedforward $F(z)$ and filter parameters would make a difference on the system stability.

As mentioned earlier, the traditional feedforward solution applies a unity feedforward gain $F(z) = 1$, hence, different sets of filter parameters and resonance frequencies have totally different system performance and stability characteristics. The robust design for LCL-filter against the grid impedance variation is discussed in next section.

C. Boundary Values for Feedforward Gain

It has been pointed out that different F values will result in different system characteristics. Although $F = 1$, is a fixed gain for traditional solution, the range that $F = 1$ belongs to can be identified through obtaining the boundaries. Two boundary values F_a and F_b can be derived by solving the inequalities in (22) to divide the whole stability region into three parts, which will be discussed in the following paragraph. The expressions of F_a and F_b are given as

$$F_a = \frac{L_1 + L_2 + L_g}{L_g} \quad (23)$$

$$F_b = \frac{L_1 + L_2 + L_g}{L_g} \cdot \frac{2 \cos(\omega_r T_s) + 1}{1 - \cos(\omega_r T_s)} \quad (24)$$

From the expressions above, F_a is a constant value whereas F_b is related to the filter resonance frequency ω_r . The F_b value has three possible options: 1) F_b is equal to or greater than F_a ; 2) F_b is greater than 0, but smaller than F_a ; and 3) F_b is less than 0. These three possibilities are shown in Fig. 9, where two special F_b boundary values need more attention: 1) F_a : If $\omega_r = \omega_s/4$, the term $\omega_r T_s$ is equal to $\pi/2$, $F_b = F_a$; 2) 0: If $\omega_r = \omega_s/3$, the term $2 \cos(\omega_r T_s) + 1 = 0$, $F_b = 0$. Therefore, the whole resonance frequency range can also be artificially divided into three regions according to which range in Fig. 9 F_b is located: a) $\omega_r \in (0, \omega_s/4)$; b) $\omega_r \in (\omega_s/4, \omega_s/3)$; c) $\omega_r \in (\omega_s/3, \omega_s/2)$.



Fig. 9. Three possible value ranges for F_b .

IV. ROBUSTNESS ANALYSIS FOR DIFFERENT RESONANCE FREQUENCIES RANGES

This part will present that different selection of resonance frequency will make a considerable difference on system stability status. System robustness against the grid inductance variation within different resonance frequency ranges are also discussed. Following previous analysis, Table II, III, IV give a comprehensive picture on how the ω_r and the gain F decide the open-loop unstable poles.

A. $\omega_r \in (0, \omega_s/4)$

In this range, $0 < F_a < F_b$. Fig. 10 plots the F_a and F_b value varying with the grid inductance L_g according to (23) and (24), where both F_a and F_b have individual limit values. With the increasing L_g value, F_a is approaching to 1 while F_b is approaching to F_{b_Lim} as given in (25), because the LCL-filter resonance frequency ω_r is approaching to ω_{LC} when the grid inductance is large enough.

$$F_{a_Lim} = 1, \quad F_{b_Lim} = \frac{2 \cos(\omega_{LC} T_s) + 1}{1 - \cos(\omega_{LC} T_s)} \quad (25)$$

where $\omega_{LC} = \sqrt{1/L_1 C}$.

Applying the Jury's criterion, Table II gives the open-loop poles number outside of unit circle in the complex plane. For $F=1$, F belongs to the range $[0, F_a]$. The number of open-loop unstable poles P is zero, which means, originally, these open loop poles are located inside the unit circle.

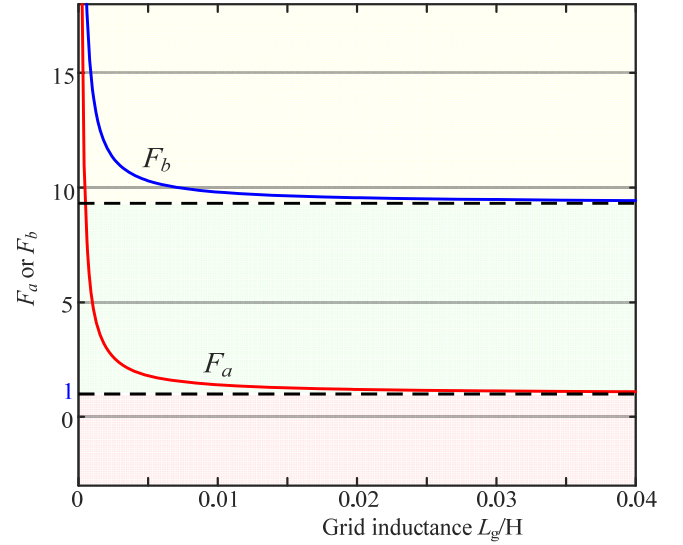


Fig. 10. F_a and F_b value under $\omega_r \in (0, \omega_s/4)$.

TABLE II
POLES DISTRIBUTION FOR DIFFERENT F SELECTIONS

$0 < \omega_r < \omega_s/4$				
F	$(-\infty, 0)$	$[0, F_a]$	$(F_a, F_b]$	$(F_b, +\infty)$
P	2	0	1	3
Status	-	no unstable open loop poles	unstable	unstable

The system stability can be preliminarily assessed by the Nyquist Stability Criterion (NSC), whose definition is formulated from the open-loop Bode diagram. Referring first to the phase response, clockwise crossing of any $\pm(2k + 1) \times 180^\circ$ line with a magnitude larger than unity or 0 dB is referred to as a positive crossing (k is an integer). Its total occurrences or number can then be denoted as N^+ . In contrast, counterclockwise crossing of the same phase line with a magnitude larger than unity is referred to as a negative crossing with its total occurrences or number notated as N^- . The NSC then states that the number of open-loop unstable poles P should be equal to $2(N^+ - N^-)$ to ensure system stability. This criterion indicates that if P is an odd number, the system will certainly be unstable. For instance, $P = 1$ or 3, the system is unstable.

According to the criterion above, the system is definitely unstable if F is selected within the ranges $(F_a, F_b]$ and $(F_a, +\infty)$ regardless of the control gain. For the range $[0, F_a]$, all the

open loop poles are located inside the unit circle, no unstable open loop poles in this range. However, the stable operation cannot be guaranteed due to the limit of control gain, whose design will be discussed in next section.

To verify the analysis above of $F=1 \in [0, F_a]$, Fig. 11 plots the open-loop and closed-loop poles distribution varying with the grid inductance L_g , respectively, where the closed-loop poles are marked with crosses while the open-loop poles are marked with the crosses inside the circle. For the open-loop poles, the GVFR ensures no open-loop poles outside of the unit circle: a pole ($z=1$) is fixed; besides, two resonant open-loop poles are pulled inside of the unit circle. This is in good agreement with the number $P=0$ given in Table II. Furthermore, according to the locus of these poles, it reveals that the GVFR offers a damping contribution to the resonance. The same conclusion is presented in [28] as well.

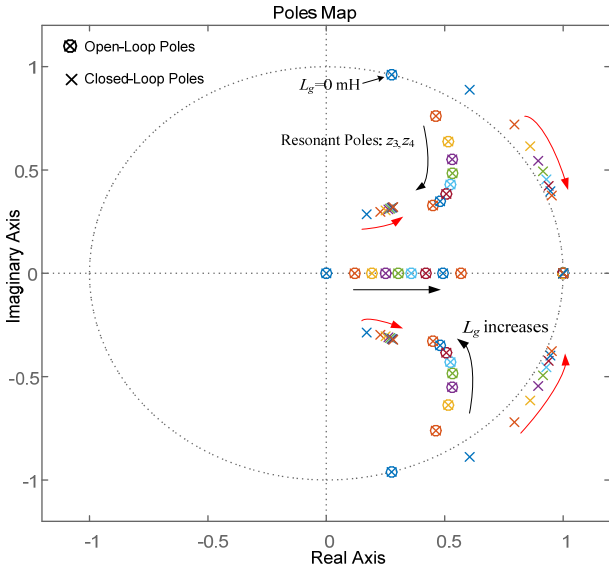


Fig. 11. Open loop and closed loop poles maps under $\omega_r \in (0, \omega_s/4)$.

B. $\omega_r \in (\omega_s/4, \omega_s/3)$

Table III presents the number of unstable open loop poles in this frequency range. Within this range, $F=1$ belongs to the range $[0, F_b]$, thus the number of open-loop unstable poles is zero, these open loop poles are located inside the unit circle.

TABLE III
POLES DISTRIBUTION FOR DIFFERENT F SELECTIONS

F	$\omega_s/4 < \omega_r < \omega_s/3$			
	$(-\infty, 0)$	$[0, F_b]$	$(F_b, F_a]$	$(F_a, +\infty)$
P	2	0	2	3
Status	-	no unstable open loop poles	-	unstable

Fig. 12 plots the F_a and F_b values varying with the grid inductance L_g , where the whole plane is divided into two parts by $\omega_r = \omega_s/4$, where the curve F_a intersects with the curve F_b ($F_a = F_b$): a) Left plane with $F_a > F_b$; b) Right plane with $F_a < F_b$, which has been discussed in previous frequency range, $\omega_r \in (0, \omega_s/4)$.

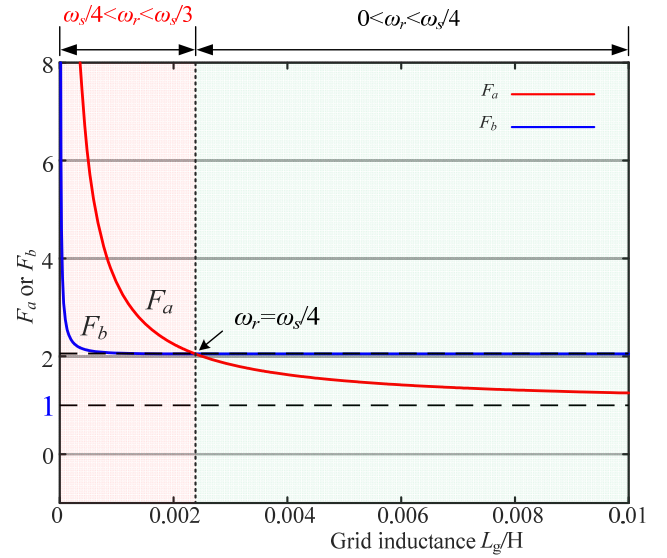


Fig. 12. F_a and F_b value under $\omega_r \in (\omega_s/4, \omega_s/3)$.

C. Robustness against grid inductance variation

As anticipated, Fig. 13 shows that there is no open-loop pole outside of the unit circle in this range. Different from the poles movement in Fig. 11, here, the closed-loop poles track directly inside the unit circle, and the increasing grid inductance value does not push the poles outside the unit circle. It means the GVFR improves the system robustness to the grid inductance variation.

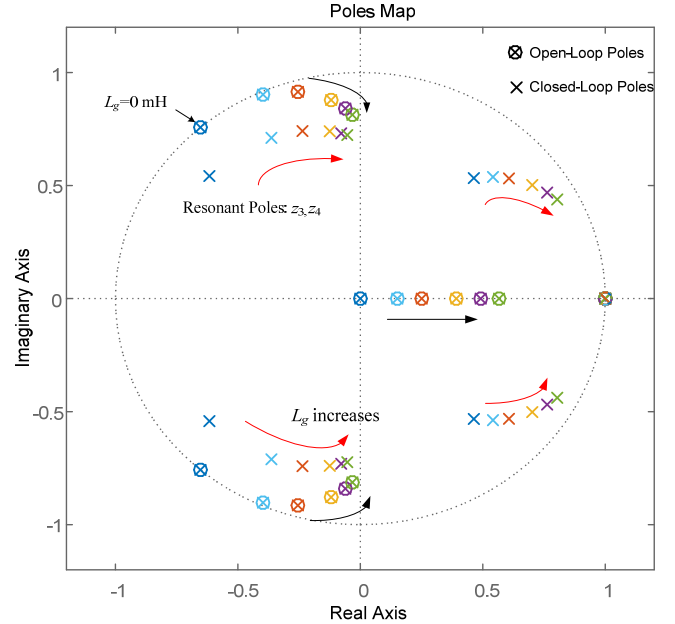


Fig. 13. Open loop and closed loop poles maps under $\omega_r \in (\omega_s/4, \omega_s/3)$.

From the figure above, it is still a question whether the poles would escape beyond the circle boundary in case of considerably large grid inductance. To figure out this query, an infinite grid inductance is assumed here.

$$L_g = +\infty \quad (26)$$

Back to equation (17) and (19), the LCL resonance frequency ω_r is approaching to ω_{LC} , k_a is equal to 1. And the $D_1(z) = 0$ is re-expressed as

$$z \cdot [z^2 - 2z \cos(\omega_{LC} T_s) + 1] - (z+1)(1 - \cos(\omega_{LC} T_s)) = 0 \quad (27)$$

$$(z-1)[z^2 + (1 - 2\cos(\omega_{LC} T_s))z + 1 - \cos(\omega_{LC} T_s)] = 0 \quad (28)$$

With further derivation, the final locations of three poles are determined through solving equation (28). If infinite grid inductance, the limits of these poles are written as

$$z_a = 1, \quad z_{b,c} = \frac{2\cos(\omega_{LC} T_s) - 1 \pm j\sqrt{3 - 4\cos^2(\omega_{LC} T_s)}}{2}, \quad 3 - 4\cos^2(\omega_{LC} T_s) > 0 \quad (29)$$

where the term under radical sign should be larger than zero. z_a is a pole tracking along the real axis. It is approaching to $z=1$ as the grid inductance increases. As for another limit poles, whether they escape beyond the circle can be judged by calculating the distance to the origin.

$$d^2 = \left(\frac{2\cos(\omega_{LC} T_s) - 1}{2} \right)^2 + \left(\frac{\sqrt{3 - 4\cos^2(\omega_{LC} T_s)}}{2} \right)^2 \quad (30)$$

$$d^2 = |1 - \cos(\omega_{LC} T_s)| \quad (31)$$

The expression of distance d is calculated as (30) and (31). In addition, the requirement that the value inside the radical in (26) should be above zero, then the sufficient condition of the distance $d < 1$ is

$$\begin{aligned} \omega_{LC} T_s < \frac{\pi}{2} &\Rightarrow \omega_{LC} < \frac{1}{4} \omega_s \text{ and } 3 - 4\cos^2(\omega_{LC} T_s) > 0 \\ &\Rightarrow \frac{1}{12} \omega_s < \omega_{LC} < \frac{5}{12} \omega_s \end{aligned} \quad (32)$$

To conclude, the system robustness will be improved if the resonance frequency of inductor L_1 and capacitor C is designed below one fourth of sampling frequency. The open loop poles are located inside the unit circle even with infinite grid impedance. It means the current loop is adaptive to the adverse grid condition with the selected design.

D. $\omega_r \in (\omega_s/3, \omega_s/2)$

In this range, $F_b < 0 < F_a$. As shown in Fig. 14, F_a and F_b approach their limit values from positive and negative infinity, respectively. Accordingly, Table IV gives the number of the open-loop poles outside the unit circle. If $F = 1$, regrettably, two unstable poles appear. In other words, the system is more likely to be unstable if the resonance frequency ω_r is higher than $\omega_s/3$.

Fig. 15 demonstrates the stability status with varying grid inductor, where (a) has only the current loop without GVFR whereas (b) equips the traditional GVFR $F = 1$.

In Fig. 15 (a), although the resonance frequency ω_r decreases according to (3) with the grid inductance increasing, the poles are still located inside the unit circle because ω_r is beyond the critical frequency. In contrast, the additional GVFR pushes these poles outside the unit circle in this frequency range, including open-loop poles and closed-loop poles. The poles distributions reveal that GVFR will destabilize the system if the resonance frequency is beyond $\omega_s/3$.

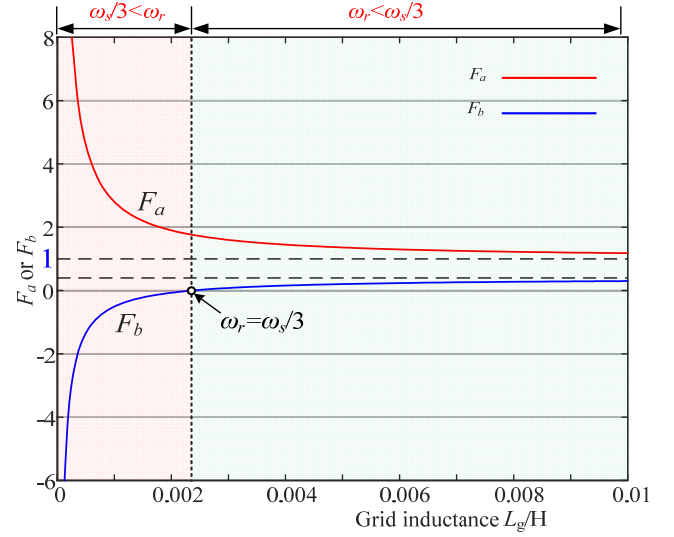
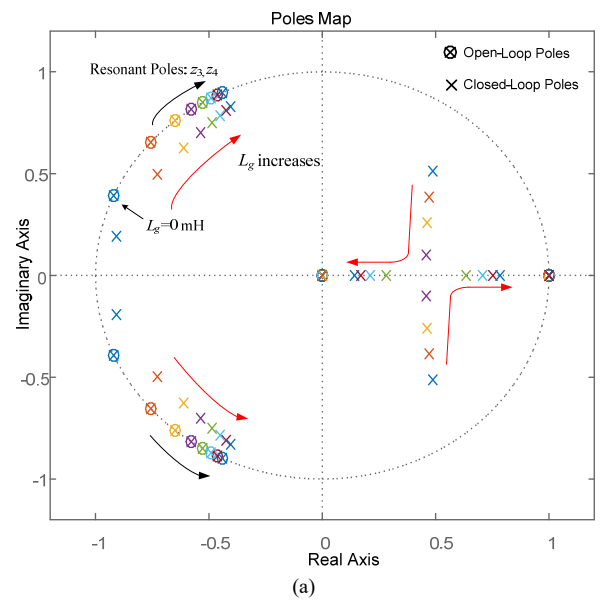


Fig. 14. F_a and F_b value under $\omega_r \in (\omega_s/3, \omega_s/2)$.

TABLE IV
POLES DISTRIBUTION FOR DIFFERENT F SELECTIONS

F	$\omega_s/3 < \omega_r < \omega_s/2$			
	$(-\infty, F_b)$	$[F_b, 0]$	$(0, F_a]$	$(F_a, +\infty)$
P	2	0	2	3
Status	-	-	-	unstable



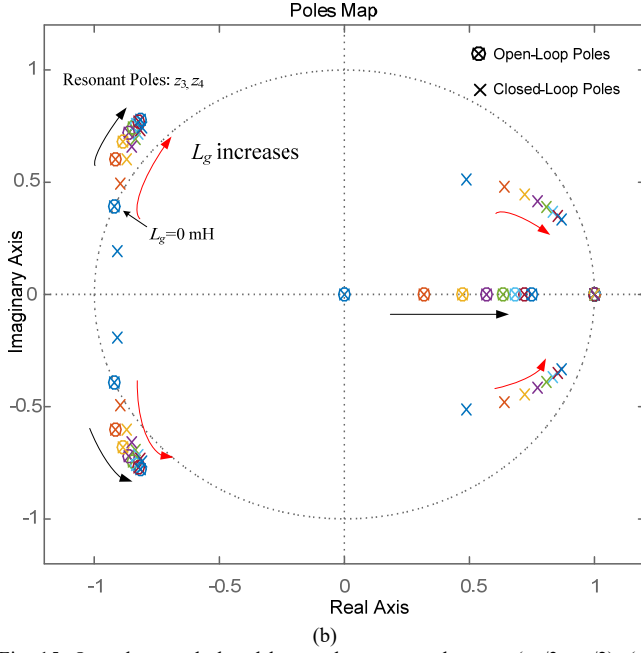


Fig. 15. Open loop and closed loop poles maps under $\omega_r \in (\omega_s/3, \omega_s/2)$: (a) without GVFR; (b) with GVFR.

E. Crossing of resonance frequency from above to below $\omega_s/3$

Uncertain grid inductance leads to varying resonance frequency of LCL-filter in a grid-interfacing inverter. Therefore, it is possible that LCL resonance frequency ω_r would vary from above to below $\omega_s/3$, resulting in the variation of stability status. Fig. 16 presented the poles movement in such a scenario. The prerequisite for this figure is that resonance frequency L_1 and C meet the requirement in (32). If the ω_r is above $\omega_s/3$, the open poles are located outside of stable boundary. During the crossing, the poles are pulled into the unit circle. The phenomenon demonstrates the analysis in previous sections.

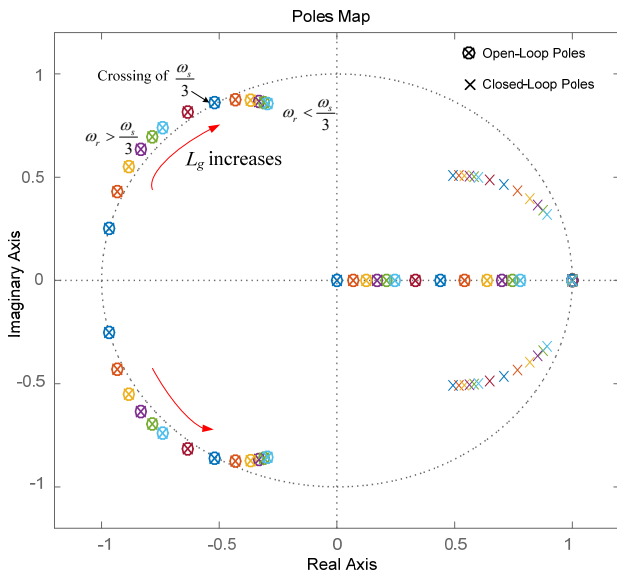


Fig. 16. Variation of resonance frequency from above to below $\omega_s/3$.

V. ROBUST DESIGN GUIDELINES FOR GRID-INTERFACING SYSTEM

As studied in previous sections, different filter parameters will significantly alter the system stability. Therefore, the selection of these parameters makes a considerable difference on system stable operation. On the other hand, the robust region of resonance frequency cannot always guarantee the stable operation because system stability also depends on the control gain and how close the actual resonance frequency has been set to the frequency boundary. In this part, a conservative but robust design recommendation for control gain and LCL resonance frequency is given and discussed.

A. Robust Selection of Filter Resonance Frequency

In a weak power system, the uncertain grid inductor L_g lead to varying LCL resonance frequencies for the voltage source inverters. According to (3), the minimum and maximum resonance frequencies can be calculated as

$$\omega_{r_min} = \omega_r|_{L_g \rightarrow \infty} = \sqrt{\frac{1}{L_1 C}}, \quad (33)$$

$$\omega_{r_max} = \omega_r|_{L_g=0} = \sqrt{\frac{L_1 + L_2}{L_1 L_2 C}}. \quad (34)$$

Already concluded in the previous section, for the investigated system, resonance frequency over the boundary $\omega_s/3$ would cause undesirable instability due to two unstable poles outside the unit circle. Although the increasing grid inductance making the frequency cross the $\omega_s/3$ may stabilize the system, it cannot guarantee stability for all possible grid inductance value. Hence, for a solid stable operation, a *conservative* design recommendation for resonance frequency ω_r is to ensure the maximum below the boundary $\omega_s/3$. Then, the resonance frequency will never go beyond the $\omega_s/3$ despite variation of grid inductor. Thus, all the open loop poles are guaranteed inside the stable boundary.

$$\omega_{r_max} < \frac{\omega_s}{3} \quad (35)$$

Besides, the damping effect of the grid voltage feedforward regulator has already been demonstrated in the range $(0, \omega_s/4)$. Therefore, if ω_r is selected above $\omega_s/6$ (the critical frequency), then the system is of course stable with certain control gain. The minimal ω_r is designed $\omega_s/6$ above to ensure that all the ω_r is above the critical frequency. On the other hand, as demonstrated in (32), to guarantee system robustness to grid inductance variation, $\omega_{r_min} < \omega_s/4$ is recommended. In summary, the filter resonance frequency can be selected as

$$\frac{\omega_s}{6} < \omega_{r_min} < \frac{\omega_s}{4} \quad (36)$$

Thus, to sum up the conditions mentioned in (32), (35) and (36), Fig. 17 presents the graphical representation of these frequency selections. The final resonance frequency can be decided according to this polar-coordinates plot.

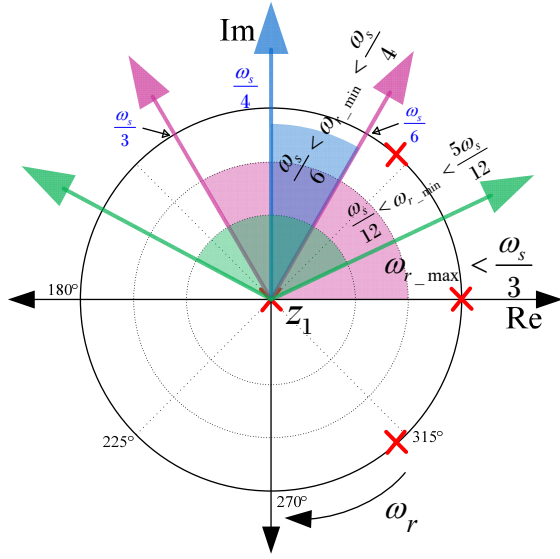


Fig. 17. Selectable area of filter resonance frequency.

B. Controller and Gain Determination

As stated previously, although the robust frequency regions are determined, the system stability also depends on the control gain. For instance, in Fig. 11, in spite of damping effect, the closed loop poles still track outside of the unit circle due to an inappropriate gain. As (13), the limit of control gain has been calculated for the individual current control loop. With the inherent damping of feedforward regulator, the control gains can be chosen directly as equation (13) to avoid complicated calculation. Fig. 18 shows the value range for the control gain within the selected frequency range. With such selection, the system stability is guaranteed.

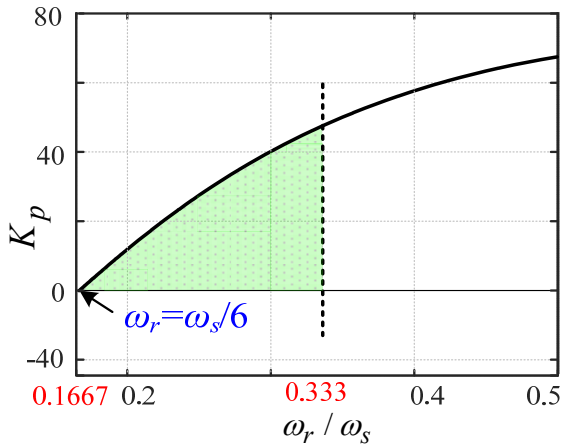


Fig. 18. Control gain limit for range $(\omega_s/6, \omega_s/3)$.

C. Determination of Filter Inductance L_1 and L_2

For the ripple in the filter inductor, the larger the inductance is, the smaller ripple exist and the lower limit is determined by the current ripple requirement. However, a large inductance will slow the system dynamic response, increase volume and

cost, also lead to a greater voltage drop on the inductor as well. Therefore, the total value of inductance ($L_T = L_1 + L_2$) should be less than 0.1 pu to limit the ac voltage drop during operation [37]. Otherwise a higher dc-link voltage will be required to guarantee current controllability, which will result in higher switching losses. The maximum value for the total inductance L_T can be written as

$$L_{T_max} \leq 10\% \cdot \frac{(v_g / \sqrt{3})^2}{\omega_0 \cdot S_0 / 3} \quad (37)$$

For two-level voltage source inverter, the maximum current ripple at the output of dc/ac inverter is [38]

$$\Delta I_{L_max} = \frac{2V_{DC}}{3L_1} (1-m) \cdot m \cdot T_s = \frac{V_{DC}}{6f_{sw}L_1}, \text{ when } m=0.5 \quad (38)$$

Calculate the minimum limitations of inductance L_1 :

$$L_1 \geq \frac{V_{DC}}{6f_{sw}\Delta I_{L_max}} \quad (39)$$

A 30% ripple of the rated current for the design parameters is assumed here, as expressed in

$$\Delta I_{L_max} = 0.3 \cdot I_{rated} = 0.3 \cdot \frac{\sqrt{2} \cdot S_0}{\sqrt{3} \cdot v_g} \quad (40)$$

Substituting (40) into (39), the minimum value of inverter-side inductance L_1 can be obtained as

$$L_1 \geq \frac{5V_{DC}v_g}{3\sqrt{6}f_{sw}S_0} \quad (41)$$

For grid-side inductance L_2 , an index N is defined as the magnitude ratio of the inverter-side current ripple to the grid-side current ripple at the switching frequency.

$$N = \left| \frac{i_l}{i_g} \right| = \frac{H_l}{H_g} = \left| L_2 C \omega_{sw}^2 - 1 \right| \quad (42)$$

where H_l and H_g are expressed as (43). The greater the N value is, the less harmonics exist in the grid-side current. N is determined by the switching frequency ω_{sw} , the inductance L_2 and filter capacitance C , L_2 can be selected once the filter capacitance C is fixed according to (42). Usually, N is greater than 20 [39].

$$H_l = \left| \frac{L_2 C s^2 + 1}{L_1 L_2 C s^3 + L_T s} \right|_{s=j\omega_{sw}}, H_g = \left| \frac{1}{L_1 L_2 C s^3 + L_T s} \right|_{s=j\omega_{sw}} \quad (43)$$

$$L_2 = \frac{N+1}{C \cdot \omega_{sw}^2} \quad (44)$$

Moreover, it is necessary to check if the sum of L_1 and L_2 is lower than the limit value in (37).

D. Selection of Filter Capacitance

The maximum limitation of filter capacitance C can be estimated by the maximum fundamental reactive power [37]

$$C_{\max} \leq \beta \cdot \frac{S_0 / 3}{\omega_0 \cdot (v_g / \sqrt{3})^2} \quad (45)$$

where S_0 is the rated power capacity of grid connected inverter, β is device fundamental reactive power index, expresses as the ratio of the acceptable maximum device fundamental reactive power to the rated power capacity, and usually set to 5% in the design. The capacitor voltage is substituted by v_g for numerical approximations.

Fig. 19 plots the selectable area of filter capacitance C , which is restricted by equation (35), (36) and maximum capacitance (45).

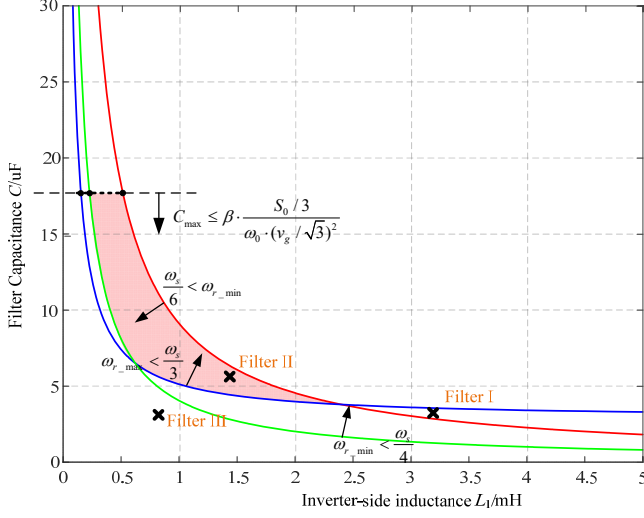


Fig. 19. Selectable area of filter capacitance C .

VI. EXPERIMENTAL RESULTS

For verification, a laboratory-scale prototype inverter with LCL-filter of Fig. 1 is built to verify the analysis. Its physical layout and parameters used are given in Fig. 20 and Table IV, respectively. The controller is implemented in a dSPACE system. A 15 kW programmable grid emulator is used to offer selectable grid voltage, and the grid impedance is replaced by an external inductor. Three different sets of LCL-filter parameters are used and given in Table VI to verify the analysis of different frequency regions in section IV, namely region 1 ($0, \omega_s/4$), region 2 ($\omega_s/4, \omega_s/3$), and region 3 ($\omega_s/3, \omega_s/2$).

TABLE V EXPERIMENTAL PARAMETERS		
NOMINAL SYSTEM PARAMETERS		
Rated capacity	S_0	10kVA
Grid frequency	f_0	50 Hz
DC-link voltage	V_{dc}	700V
Switch frequency	f_{sw}	10 kHz
Grid voltage (p-p)	v_g	300Vrms

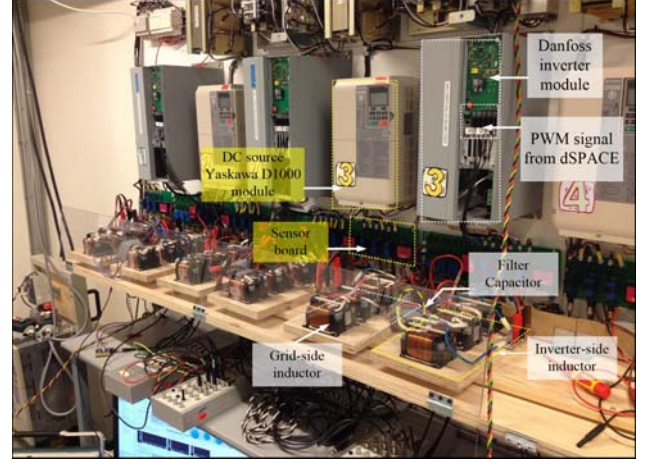


Fig. 20. Laboratory-scale experimental prototype.

TABLE VI
EXPERIMENTAL PARAMETERS

Parameters of Filter I		
Converter inductor	L_1	3.2 mH
Filter capacitor	C	3 uF
Grid-side inductor	L_2	0.8 mH
Grid inductance	L_g	1.5 mH
Resonance	f_r	2.51 kHz
Parameters of Filter II		
Converter inductor	L_1	1.5 mH
Filter capacitor	C	6 uF
Grid-side inductor	L_2	0.8 mH
Grid inductance	L_g	0.8 mH
Resonance	f_r	2.34 kHz
Parameters of Filter III		
Converter inductor	L_1	0.8 mH
Filter capacitor	C	3 uF
Grid-side inductor	L_2	0.8 mH
Grid inductance	L_g	0.8 mH
Resonance	f_r	3.98 kHz

At first, the parameters of Filter I are chosen, which is actually outside the robust area set in Fig. 19. Because its resonance frequency is close to the critical frequency. Here, the sampling frequency is selected as 20 kHz, whose critical frequency equalizes to 3.33 kHz. Fig. 21 (a) shows the experimental waveforms, where the system is originally stable in a stiff grid. Obviously, such a system is not robust to grid inductance variation. As shown in Fig. 21 (b), the system becomes undesirably oscillatory when the grid impedance is inserted. An external grid inductance L_g is added to emulate the weak power system. Fig. 21 (c) shows the result that the system returns to stable if the GVFR is enabled. It demonstrates the damping effects of the feedforward scheme on the LCL-filter resonance for the region 1 case, which has been concluded in previous section.

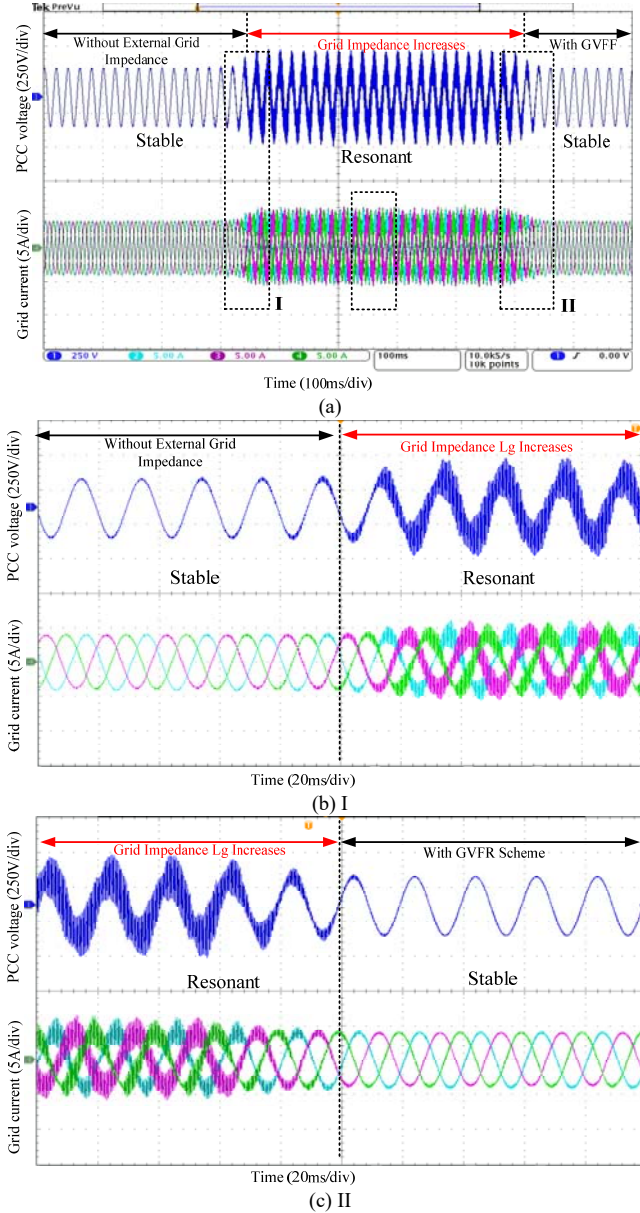


Fig. 21. Measured grid current and PCC voltage waveforms for frequency region 1 (a) full time scale, (b) grid impedance makes the system unstable, (c) the GVFR scheme is added.

Following the above case, Fig. 22 shows the experimental waveforms with the Filter II parameters given in Table VI, located right inside the robust area in Fig. 19. Such a system should be more robust to different grid conditions. All resonance frequencies in this range are above the critical frequency, hence the system can work stable without damping. The sampling frequency is selected as 10 kHz, whose critical frequency equalizes to 1.67 kHz. To verify the damping effect, the dynamic responses are compared. A step change in the reference from 2.5 to 5A is set to demonstrate the dynamic performance and potentially excite any resonance that may occur. Fig. 22 (a) shows the experimental response for the case without GVFR. The system is clearly still quite stable, but has insufficient damping, as displayed by the slight oscillatory response just after the transient step. Comparatively, Fig. 22 (b)

shows the result for the case with GVFR. It is clear that almost no oscillations can be observed during the transient, which confirms the theoretical analysis.

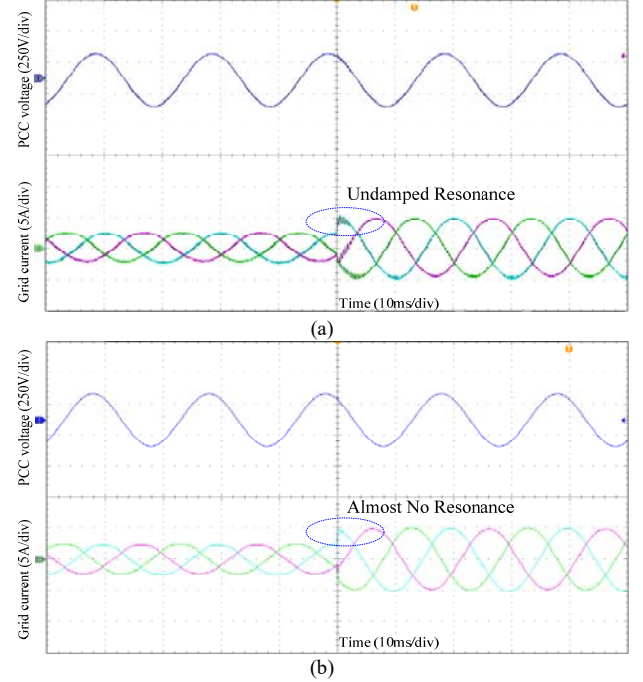


Fig. 22. Measured grid current and PCC voltage waveforms for frequency region 2 (a) grid current step change from 2.5A to 5A without GVFR; (b) grid current step change from 2.5A to 5A with GVFR.

Similar experiments are carried out for the Filter III parameters, which is also outside the robust area. Note that the system will be stable without additional damping for this frequency range. Fig. 23 shows the experimental waveforms when the GVFR scheme is employed in this situation. This is in agreement with the poles map shown in Fig. 15, where the resonant poles are located just outside the unit circle and, thus, describe a system that is underdamped and unstable.

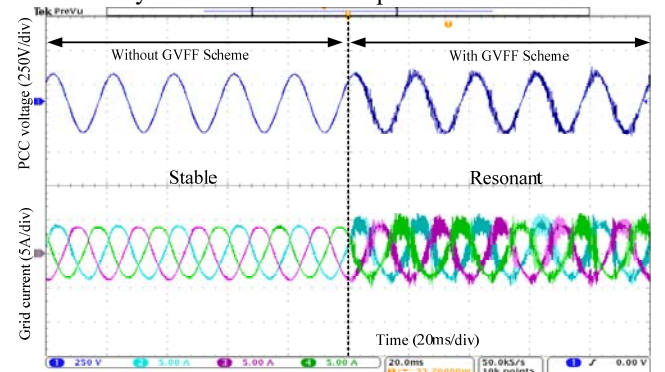


Fig. 23. Measured grid current and PCC voltage waveforms for frequency region 3 with unit proportional GVFR scheme.

VII. CONCLUSION

This paper comprehensively analyzes the stability and robustness of a grid-interfacing inverter with LCL-filter in the discrete domain, where the LCL-filter, along with the controller, are modeled in a polar coordinate. System open-loop and closed-loop poles are analytically studied and

expressed in the z -domain. The critical frequency of LCL-filter is mathematically identified through the system control gain expression. In a weak grid, two more boundary frequencies are revealed through the Jury stability criterion. The robustness analysis suggests a frequency range for the resonance frequency of inductor L_1 and capacitor C . Finally, to improve the robustness against grid inductance variation, a conservative design recommendation of filter parameters and control gain is given. Through the tests on a laboratory-scale prototype, the theoretical analysis is validated by experimental results.

REFERENCES

- [1] X. Wang, F. Blaabjerg, and W. Wu, "Modeling and analysis of harmonic stability in an AC power-electronics-based power system," *IEEE Trans. Power Electron.*, vol. 29, no. 12, pp. 6421–6432, Dec. 2014.
- [2] M. Lu, X. Wang, P.C. Loh, F. Blaabjerg, "Resonance Interaction of Multi-Parallel Grid-Connected Inverters with LCL Filter," *IEEE Trans. on Power Electron.*, vol. 32, no. 2, pp. 894–899, Feb. 2017.
- [3] E. Twining and D. G. Holmes, "Grid current regulation of a three-phase voltage source inverter with an LCL input filter," *IEEE Trans. Power Electron.*, vol. 18, no. 3, pp. 888–895, May 2003.
- [4] R. Teodorescu, F. Blaabjerg, M. Liserre, and A. Dell'Aquila, "A stable three-phase LCL-filter based active rectifier without damping," in *38th IAS Annu. Meeting. Ind. Applicat. Conf. Rec.*, 2003, vol. 3, pp. 1552–1557.
- [5] M. Lu, F. Blaabjerg, X. Wang, "Interaction admittance based modeling of multi-paralleled grid-connected inverter with LCL-filter," in *Proc. of 2016 IEEE 2nd Annual Southern Power Electronics Conference (IEEE SPEC 2016)*, Auckland, NZ, Dec. 2016, pp. 1–7.
- [6] J. Agorreta, M. Borrega, J. Lopez, and L. Marroyo, "Modeling and control of N-paralleled grid-connected inverters with LCL filters coupled due to grid impedance in PV plants," *IEEE Trans. Power Electron.*, vol. 26, no. 3, pp. 770–1194, Mar. 2011.
- [7] Y. Jia, J. Zhao, and X. Fu, "Direct grid current control of LCL-filtered grid-connected inverter mitigating grid voltage disturbance," *IEEE Trans. Power Electron.*, vol. 29, no. 3, pp. 1532–1541, Mar. 2014.
- [8] Z. Xin, X. Wang, P.C. Loh, F. Blaabjerg, "Grid-current feedback control for LCL-filtered grid converters with enhanced stability," *IEEE Trans. Power Electron.*, vol. 32, no. 4, pp. 3216–3228, Apr. 2017.
- [9] D. Pan, X. Ruan, X. Wang, H. Yu and Z. Xing, "Analysis and Design of Current Control Schemes for LCL-Type Grid-Connected Inverter Based on a General Mathematical Model," *IEEE Trans. Power Electron.*, vol. 32, no. 6, pp. 4395–4410, Mar. 2011.
- [10] Y. Tang, P. C. Loh, P. Wang, F. H. Choo, and F. Gao, "Exploring inherent damping characteristic of LCL-filters for three-phase grid-connected voltage source inverters," *IEEE Trans. Power Electron.*, vol. 27, no. 3, pp. 1433–1443, Mar. 2012.
- [11] J. Yin, S. Duan, B. Liu, "Stability analysis of grid-connected inverter with LCL filter adopting a digital single-loop controller with inherent damping characteristic," *IEEE Trans. Ind. Inf.*, vol. 9, no. 2, pp. 1104–1112, May. 2013.
- [12] A. Kahrobaian and Y. A. I. Mohamed, "Robust single-Loop direct current control of LCL-filtered converter-based DG units in grid-connected and autonomous microgrid modes," *IEEE Trans. Power Electron.*, vol. 29, no. 10, pp. 5605–5619, Oct. 2014.
- [13] S.G. Parker, B. P. McGrath, D.G. Holmes, "Regions of Active Damping Control for LCL Filters," *IEEE Trans. Ind. Appl.*, vol. 50, no. 1, pp. 424–432, Jan./Feb. 2014.
- [14] C. Zou, B. Liu, S. Duan, R. Li, "Influence of delay on system stability and delay optimization of grid-connected inverters with LCL filter," *IEEE Trans. Ind. Inf.*, vol. 10, no. 3, pp. 1175–1184, Aug. 2014.
- [15] J. Wang, J. D. Yan, L. Jiang, and J. Zou, "Delay-dependent stability of single-loop controlled grid-connected inverters with LCL filters," *IEEE Trans. Power Electron.*, vol. 31, no. 1, pp. 743–757, Jan. 2016.
- [16] D. Pan, X. Ruan, C. Bao, W. Li, and X. Wang, "Optimized controller design for LCL-type grid-connected inverter to achieve high robustness against grid-impedance variation," *IEEE Trans. Ind. Electron.*, vol. 62, no. 3, pp. 1537–1547, Mar. 2015.
- [17] L. Harnefors, A. G. Yepes, A. Vidal, and J. D. Gandoy, "Passivity-based controller design of grid-connected VSCs for prevention of electrical resonance instability," *IEEE Trans. Ind. Electron.*, vol. 62, no. 2, pp. 702–710, Feb. 2015.
- [18] X. Li, X. Wu, Y. Geng, X. Yuan, C. Xia, and X. Zhang, "Wide damping region for LCL-type grid-connected inverter with an improved capacitor-current-feedback method," *IEEE Trans. Power Electron.*, vol. 30, no. 9, pp. 5247–5259, Sep. 2015.
- [19] M. Lu, X. Wang, P.C. Loh, F. Blaabjerg, T. Dragicevic, "Graphical Evaluation of Time-Delay Compensation Techniques for Digitally Controlled Converters," *IEEE Trans. on Power Electron.*, Early access, Mar. 2017.
- [20] D. Yang, X. Ruan, and H. Wu, "Impedance shaping of the grid-connected inverter with LCL filter to improve its adaptability to the weak grid condition," *IEEE Trans. Power Electron.*, vol. 29, no. 11, pp. 5795–5805, Nov. 2014.
- [21] R. Teodorescu, F. Blaabjerg, M. Liserre, et al, "Proportional-resonant controllers and filters for grid-connected voltage-source converters," *IEEE Proceedings Electron. Power Appl.*, 2006, 153 (5): 750–762.
- [22] H. Zhou, Y. Li, N.R. Zargari, "Selective harmonic compensation (SHC) PWM for gridinterfacing high-power converters," *IEEE Trans. Power Electron.*, vol. 29, no. 3, pp. 1118–1127, Mar. 2014.
- [23] R. Teodorescu, F. Blaabjerg, U. Borup, and M. Liserre, "A new control structure for grid-connected LCL PV inverters with zero steady-state error and selective harmonic compensation," in *Proc. IEEE APEC*, 2004, vol. 1, pp. 580–586.
- [24] T. Abeyasekera, C. M. Johnson, D. J. Atkinson, and M. Armstrong, "Suppression of line voltage related distortion in current controlled grid connected inverters," *IEEE Trans. Power Electron.*, vol. 20, no. 6, pp. 1393–1401, Nov. 2005.
- [25] X. Wang, X. Ruan, S. Liu, and C. K. Tse, "Full Feedforward of Grid Voltage for Grid-Connected Inverter With LCL Filter to Suppress Current Distortion Due to Grid Voltage Harmonics," *IEEE Trans. Power Electron.*, vol. 25, pp. 3119–3127, 2010.
- [26] M. Xue, Y. Zhang, Y. Kang, Y. Yi, S. Li, and F. Liu, "Full feedforward of grid voltage for discrete state feedback controlled grid-connected inverter with LCL filter," *IEEE Trans. Power Electron.*, vol. 27, no. 10, pp. 4234–4247, Oct. 2012.
- [27] Y. Zhang, M. Xue, M. Li, and Y. Kang, "Co-design of the LCL filter and control for grid-connected inverters," *Journal of Power Electronics*, vol. 14, no. 5, pp. 1047–1056, Sep. 2014.
- [28] M. Lu, X. Wang, F. Blaabjerg, S.M. Mueen, "Grid-voltage-feedforward active damping for grid-connected inverter with LCL filter," in *Proc. IEEE APEC*, 2016, vol. 1, pp. 1941–1946.
- [29] C. Zou, B. Liu, S. Duan, and R. Li, "A feedforward scheme to improve system stability in grid-connected inverter with LCL filter," in *Proc. IEEE Energy Convers. Congr. Expo.*, 2013, pp. 4476–4480.
- [30] J. Wang, Y. Song, A. Monti, "A study of feedforward control on stability of grid-parallel inverter with various grid impedance," in *Proc. IEEE 5th International Symposium on Power Electronics for Distributed Generation Systems (PEDG)*, pp. 1–8, June 2014.
- [31] X. Li, J. Fang, Y. Tang, X. Wu and Y. Geng, "Capacitor voltage feedforward with full delay compensation to improve weak grids adaptability of LCL-filtered grid-connected converters for distributed generation systems," *IEEE Trans. Power Electron.* 2017, in press.
- [32] B. S. Buso and P. Mattavelli, "Digital control in power electronics," in *Synthesis Lectures on Power Electronics*. San Rafael, CA: Morgan & Claypool, 2006.
- [33] M. Liserre, R. Teodorescu, F. Blaabjerg, "Stability of Photovoltaic and Wind Turbine Grid-Connected Inverters for a Large Set of Grid Impedance Values," *IEEE Trans. Power Electron.*, vol. 21, no. 1, pp. 263–272, Jan. 2006.
- [34] E. I. Jury, *Theory and Application of the Z-Transform Method*. New York: Wiley, 1964.
- [35] E. Jury, "A simplified stability criterion for linear discrete systems," *Proc. IRE*, vol. 50, no. 6, pp. 1493–1500, 1962.
- [36] E. I. Jury, *Theory and Application of the Z-Transform Method*. New York: Wiley, 1964.
- [37] M. Liserre, F. Blaabjerg, and S. Hansen, "Design and control of an LCL filter-based three-phase active rectifier," *IEEE Trans. Ind. Appl.*, vol. 41, no. 5, pp. 1281–1291, Sep./Oct. 2005.
- [38] A. Reznik, M. Simoes, A. Al-Durra, and S. Mueen, "LCL filter design and performance analysis for grid-interconnected systems," *IEEE Trans. Ind. Appl.*, vol. 50, no. 2, pp. 1225–1232, Mar. 2014.

- [39] Q. Liu, L. Peng, Y. Kang, "A Novel Design and Optimization Method of an LCL filter for a shunt Active Power Filter," *IEEE Trans. Ind. Electron.*, vol. 61, no. 8, pp. 4000-4010, Aug. 2014.